

Compact Binaries through a Lens: Silent vs. Detectable Microlensing for the LIGO-Virgo-KAGRA Gravitational Wave Observatories

Ruxandra Bondarescu,^{*} Helena Ubach,[†] and Oleg Bulashenko[‡]
*Institut de Ciències del Cosmos (ICCUB), Facultat de Física,
 Universitat de Barcelona, Martí i Franquès 1, E-08028 Barcelona, Spain*

Andrew Lundgren[§]
*Institute of Cosmology and Gravitation, University of Portsmouth,
 Dennis Sciama Building, Burnaby Road, Portsmouth, PO1 3FX, United Kingdom*
 (Dated: November 28, 2022)

Massive objects located between Earth and a compact binary merger can act as a magnifying glass improving the sensitivity of gravitational wave detectors to distant events. A point mass lens between the detector and the source can manifest itself either through an amplification of the gravitational wave signal in a frequency dependent manner that is maximum at merger or through magnification combined with the appearance of a second image that interferes with the first creating a regular, predictable pattern. We map the increase in the signal to noise ratio for upcoming LVK observations as a function of the mass of the lens M_L and dimensionless source position y for any point mass lens between the detector and the binary source. We find that most microlensing is silent with mismatch under 10% and may never be identified as lensed. To quantify detectability, we compute the optimal match between the lensed waveform and the waveforms in the unlensed template bank and provide a map of the match. The higher the mismatch with unlensed templates, the more detectable lensing is. Furthermore, we estimate the probability of lensing, and find that the redshift to which binary mergers are visible with the LVK increases from $z \approx 1$ to $z \approx 3.2$ for a total detected mass $M_{det} = 120M_\odot$. The overall probability of lensing is $< 20\%$ of all detectable events above the threshold SNR for $M_{det} = 120M_\odot$ and $< 5\%$ for more common events with $M_{det} = 60M_\odot$. We find that there is a selection bias for detectable lensing that favors events that are close to the line of sight $y \lesssim 0.5$. Black hole binary searches could thus improve their sensitivity by introducing a prior that takes the bias into account. The match, the SNR increase due to lensing, and the probability of lensing are weakly dependent on the noise curve of the detector with very similar results for both the O3 and predicted O4 noise power spectral densities.

I. INTRODUCTION

Gravitational wave detectors register oscillations in the fabric of space-time, which propagate at the speed of light. These waves are not absorbed by intervening matter providing a unique insight into the dynamics of the universe. Since the spacetime is very stiff, gravitational waves are very weak, and can only be detected on Earth if they come from the inspiral and merging of very dense compact objects like binary black holes or neutron stars. Black holes have the strongest gravitational wave emission and can be detected further away than other compact objects. This makes them more likely candidates for gravitational lensing, where an object close to the line of sight interposes between the source and the detector amplifying the gravitational wave emission. While black holes are fully characterized by mass, spin and charge, the emitted gravitational waves from a binary merger represent the last act in a million or billion year chain of events. Reconstructing the characteristics of the binary

in the source frame where the collision happened is the primary challenge after the identification of the signal.

The first merging black holes detected from the emitted gravitational radiation were unlike any black holes seen in the Milky Way before. They are quite massive, substantially more than black holes found in X-ray studies, and appear not to have much spin. Since the first detection in 2015 [1], the LIGO-Virgo-Kagra (LVK) collaboration has registered about 90 gravitational wave events [2–4]. The average total mass for detected gravitational wave binaries is $M_{det} \approx 60M_\odot$, which is unexpectedly high. One proposed explanation for such high masses is gravitational lensing [5, 6].

While gravitational wave signals provide information that is complementary to telescope observations, they are challenging to interpret correctly. Massive objects within an Einstein cone of the detected compact object collision alter the signal causing gravitational lensing [7, 8]. It can result in magnified signals, duplicate events, or conspire to create a beating pattern in the waveform which occurs when the time delay between the paths is comparable with the period of the wave. Repeated events separated by minutes to months occur when the lens is a galaxy [9–13]. The separation can increase up to years for galaxy clusters [14–16]. Here we focus on microlensing by stars or other compact objects (duplicate events separated by milliseconds to seconds). Microlensing in the context of

^{*} ruxandra@icc.ub.edu

[†] helenaubach@icc.ub.edu

[‡] oleg@fqa.ub.edu

[§] andrew.lundgren@port.ac.uk

gravitational waves has been the focus of a plethora of studies [5, 6, 17–36].

Careful modeling can turn gravitational lensing from a hindrance in waveform recovery to a new instrument in gravitational wave astrophysics. Some gravitational lenses could be objects that do not emit light or neutrinos and cannot be observed through other channels. Lensing could then constrain populations of unknown or poorly understood objects like intermediate mass black holes [22, 37], dark matter haloes [38–40] or topological defects [41–43] and even prove the existence of new objects. When we compute the number of lenses we take the amount of dark matter in the universe split into microlenses as an upper limit. A first detection of gravitational lensing could provide the first direct evidence of compact dark matter objects [38, 39, 44–49].

The lensing amplification causes the source’s distance from the detector to be underestimated. Not only does it appear to be closer, but it also appears more massive because the redshift is underestimated. It is thus crucial to determine whether a detected gravitational wave signal is lensed or not, because misidentification results in wrong parameter estimation, e.g., if the signal is magnified due to the presence of massive objects in between the binary inspiral and Earth it will appear further than it actually is. A binary at $z = 3$ will appear four times more massive when detected $M_{\text{det}} = (1 + z)M_{\text{src}}$. A population of objects with suspicious distances or masses could provide indirect evidence of lensing. *In this paper we ask the questions of when microlensing of an individual source can be clearly detected, and how would such a detection appear.* Characteristics of lensing include (1) the appearance of a second image, (2) a regular pattern of minima and maxima that is predictable or simply (3) an amplification of the signal that increases with frequency and is maximum at merger.

While the LVK collaboration analyzed O2, O3a and O3b observation runs [50–52], they did not find confident evidence for gravitational-wave lensing. However, the detectors will be online soon with improved sensitivity. The detection rate is expected to increase from one gravitational wave per week in O3 to a possible one per day in O4 [53]. The higher number of sources elevate the probability of detecting a detectably lensed event. Furthermore, plans for new, advanced detector facilities are crystalizing in both Europe via the Einstein Telescope and the US via the Cosmic Explorer [54–57].

Here we investigate scenarios for detection of microlensing of binary black hole coalescences. Sec. II begins by reviewing the effect of a point-mass lens (PML) on the gravitational-wave signal. The point-mass lens is the simplest most illustrative model for a microlensing object. The lensing effects depend only on the lens mass M_L and y , which gives the position of the lens relative to the line of sight between the source and the detector. We compute the relative increase in the signal-to-noise ratio (SNR) caused by the lensing amplification of the signal, which induces detectability to larger distances and show

that it is similar for O3 and O4 noise curves. The parameter space is divided in three regions: the amplification region (the SNR increase depends only on M_L), a transition region (the SNR increase depends on both y and M_L), and the geometrical optics region (the oscillations in the transmission factor average out, and the SNR increase depends only on y).

In Sec. III the mismatch of the lensed signal versus unlensed signals is calculated. It quantifies how much SNR is needed to distinguish the signals from each other. We quantify the detectability by the mismatch of the lensed signal versus any unlensed templates. This is the fundamental ingredient in model comparisons, and without sufficient mismatch the signal intrinsically does not contain information to indicate that it is lensed. Sec. IV proceeds by showing the impact of lensing on the waveform in both the time and frequency domain.

Crucially, Sec V evaluates not just the rate of lensing, but the rate of *detectable* lensing. Otherwise, lensing is *silent*. In silent lensing, the distance to the binary and the mass of the binary could be affected without creating a detectable mismatch with unlensed templates. Selecting only for lensed waveforms that carry enough of a lensing imprint to be measured limits parameter space improving prior distribution of lens parameters for detecting microlensing.

The straightforward approach to detecting microlensing is to do Bayesian parameter estimation of individual events with lensing added to the waveform model. This requires also prior distributions for the lens mass M_L and the dimensionless lens angle y . The obvious choice for priors is to model the distribution of lenses expected to exist in the universe. For the angle this is simple because randomly distributed lenses will follow a scale-free distribution $p(y) \propto y dy$ regardless of lens mass. The difficulty is that this puts the most weight on lenses farthest from the line of sight, which have a negligible effect on the signal. Even if an artificial limit is put on y , the prior most heavily weights lenses at the boundary, and the Bayesian estimate will be biased most toward systems that are not meaningfully lensed.

Our proposed solution is to condition our prior on the fact that the source must be detected above a given SNR threshold. Any sources too far away to be detected are not considered. This selection bias reshapes the prior on the lensing parameters. Lenses closer to the line of sight cause more amplification, increasing the sensitive volume and enhancing their relative rate of detections. This prior incorporates more of our knowledge and is therefore closer to optimal for the detection of lensing.

We note that the effect of lensing depends on the redshifted lens mass, while the most natural prior gives our belief about the mass of the lens in its own frame. Hence there is an extra variable, the lens distance, which must be tracked. Our approach naturally incorporates this as well. However, in this first paper, we do not include a specific model that predicts the number and masses of lenses since they are so uncertain. We leave that to future

work. Instead we show the priors when they are conditioned as well on the lensed waveform having a sufficient mismatch that it leaves a measurable imprint on the signal. Conclusions and future directions are presented in Sec. VI.

II. POINT MASS LENS

All massive astrophysical objects are potential lenses that can be encountered by a passing gravitational wave. For gravitational lensing the point mass lens model (PML) is valid when the dimension of the lens is much smaller than the Einstein radius, e.g., for black holes, dense dark matter clumps, etc. Due to its simplicity, the PML model has been used in the literature for interpreting both electromagnetic [7, 8, 58, 59] and gravitational wave lensing [17–26, 29–39, 44, 46–49].

Generally, lensing effects become significant when the source, the lens and the observer are all aligned within the Einstein angle $\theta_E = R_E/d_L$, i.e., the lens is located near the line of sight. The line of sight is defined as the line joining the observer and the center of the lens. The Einstein radius is given by

$$R_E = \sqrt{2\mathcal{R}_S d_{LS} d_L/d_S}, \quad (1)$$

which is much smaller than the angular diameter distances d_L , d_S and d_{LS} from the lens to the observer, from the source to the observer, and between the lens and the source, respectively. Here $\mathcal{R}_S = 2GM_L/c^2$ is Schwarzschild radius of the lens, which is directly proportional to the mass of the lens M_L .

A. Transmission Factor

Since lensing occurs in a relatively narrow region compared to the cosmological distances traveled by the wave (d_L , d_S and d_{LS}), the transmission factor can be computed in the thin lens approximation. The lens mass can then be projected onto a lens plane. In this approximation, the gravitational waves propagate freely outside the lens and interact only with a two-dimensional gravitational potential at the lens plane, where their trajectory is suddenly modified via the transmission factor F . For the PML it is given by [7, 58]

$$F = e^{\frac{1}{2}\pi^2\nu} e^{i\pi\nu \ln(\pi\nu)} \Gamma(1 - i\pi\nu) {}_1F_1(i\pi\nu; 1; i\pi\nu y^2), \quad (2)$$

where $\nu \equiv ft_M$ is the frequency of the gravitational wave f scaled by the characteristic time t_M , $\Gamma(z)$ is the Gamma function, and ${}_1F_1(a, b, z)$ is the confluent hypergeometric function. The transmission factor represents the ratio between the lensed wave field received by the observer, and the unlensed one (what would be observed when no lens was present). Our transmission factor is the complex conjugate of that in some other works, but is appropriate to the sign convention that we use for Fourier transforms.

As seen from Eq. (2), the transmission factor, which is a function of frequency, depends on two parameters:

- the mass of the lens M_L through the time

$$t_M = 2\mathcal{R}_S/c \approx 2 \times 10^{-5} \text{ s } (M_L/M_\odot), \quad (3)$$

- the scaled offset of the source

$$y = \theta_S/\theta_E, \quad (4)$$

where θ_S is the angular position of the source with respect to the line of sight, and $\theta_E = R_E/d_L$ is the Einstein angle.

The strain of the lensed gravitationally signal $\tilde{h}(f)$ (that would finally be detected) is the product of the unlensed strain $\tilde{h}_{UL}(f)$ and the transmission factor $F(f)$ in the frequency domain:

$$\tilde{h}(f) = \tilde{h}_{UL}(f) \cdot F(f). \quad (5)$$

We are interested in the behavior of the transmission factor for the frequency region the LVK is sensitive to, which begins at about 15 Hz and ends at merger for the BH binaries considered here.

The absolute value of the transmission factor is obtained from Eq. (2) as follows [58]

$$|F| = \left(\frac{2\pi^2\nu}{1 - e^{-2\pi^2\nu}} \right)^{1/2} |{}_1F_1(i\pi\nu; 1; i\pi\nu y^2)|. \quad (6)$$

Its behavior has already been described in the literature [19, 20, 58] (in the current notations, see also Ref. [36]). Here, we briefly review the main features which will be necessary for further analysis.

The transmission factor starts from $|F| \approx 1$ at small ν . Then, for a fixed source position y , it grows monotonically as a function of frequency before its first maximum (see Fig. 1). This is the *amplification region* for which wave optics dominates. In this region, the transmission factor is independent of y , as can be seen from Fig. 1, and it matches an asymptotic formula [58]

$$|F|_{\text{amp}} = \left(\frac{2\pi^2\nu}{1 - e^{-2\pi^2\nu}} \right)^{1/2} \approx (2\pi^2\nu)^{1/2}. \quad (7)$$

The extension of the amplification region depends on the lens mass: the lower M_L , the higher the frequency when the signal starts to be magnified due to lensing. On the other hand, the level of magnification is determined by the lens alignment y .

For higher frequencies, the transmission factor starts to oscillate (see Fig. 1) approaching the *geometrical optics* (GO) region, where the dominant contribution comes from two well-defined images of the source. In this limit, the transmission factor is given by

$$|F|_{\text{GO}} = \left(\frac{y^2 + 4 \cos^2 \alpha}{y \sqrt{y^2 + 4}} \right)^{1/2}, \quad (8)$$

where $\alpha = \pi f \Delta t_{21} - \pi/4$. It oscillates between regular, predictable maxima and minima that correspond to constructive and destructive interference caused by the time delay Δt_{21} between the two images and an additional Morse (topological) phase shift. For the close alignment condition ($y \lesssim 0.5$), $\Delta t_{21} \approx 2y t_M$ and the position of each oscillation occurs at known frequencies [36]

$$f_n = \Delta f \cdot \begin{cases} (n + \frac{1}{4}), & \text{at maxima,} \\ (n + \frac{3}{4}), & \text{at minima.} \end{cases} \quad (9)$$

with $n = 0, 1, 2, \dots$ and the frequency spacing

$$\Delta f = \frac{1}{2 t_M y} \simeq 2.5 \times 10^4 \text{ Hz} \left(\frac{M_\odot}{M_L} \right) \left(\frac{1}{y} \right). \quad (10)$$

The onset of the GO oscillations can be assigned to a threshold frequency f_G between the first maximum and the first minimum, that gives $f_G \Delta t_{21} \approx 1/2$ [36].

We emphasize that

(i) the lensing oscillations occur at predictable frequencies and are equally spaced in frequency with Δf corresponding to the inverse of the time delay Δt_{21} between the two images [Eqs. (9) and (10)];

(ii) the amplitude of maxima and minima stays constant when y is fixed, which can be seen in Fig. 1 as dotted horizontal lines:

$$|F|_{GO}^{\max} = \left(\frac{\sqrt{y^2 + 4}}{y} \right)^{1/2}, \quad |F|_{GO}^{\min} = \left(\frac{y}{\sqrt{y^2 + 4}} \right)^{1/2}. \quad (11)$$

Note, the closer the source to the line of sight (i.e. the smaller y), the higher the maximum amplification, $|F|_{GO}^{\max}$.

(iii) in the “close alignment” regime, $y \lesssim 0.5$, the spacing of the oscillations will be given by the inverse of the product $2y t_M$, while the amplification of the maxima and minima will be given by $|F|_{GO}^{\max} \approx 2/y + y/4$ and $|F|_{GO}^{\min} \approx y/2$ [36].

These remarks are important, since the effect of the oscillations on the waveform $\tilde{h}_{UL}(f)$ can be commonly mistaken by other “mimickers” like precession [60, 61] or eccentricity [62]. For these, the waveform is modulated at the source, while the lens modulates the waveform on its way to the observer. The regular spacing of the oscillations is characteristic to the lensing effect and is related to the phase difference (including a Morse phase shift) between the two GO paths. Knowing that the oscillations are equally spaced could be one way to distinguish the lensing case from the “mimickers” when enough of the signal is detected. As a comparison, precession does not induce regularly spaced oscillations – there the oscillations are more pronounced at low frequencies [60, 61].

For a given choice of parameters M_L and y , the lensing effect on GWs in the LVK range (shown by vertical dashed lines in Fig. 1) can fall into the GO oscillating region, the amplification region, or into the intermediate part, depending on the lens mass, as seen in Fig. 1.

If the mass is very low (e.g. $M_L = 30 M_\odot$), the effect will be mainly amplification. If the mass is higher, then oscillations will appear. The spacing of the oscillations will depend on the product $y t_M$ [Eq. (10)], while the amplification of the maxima and minima will be only dependent on y [Eq. (11)].

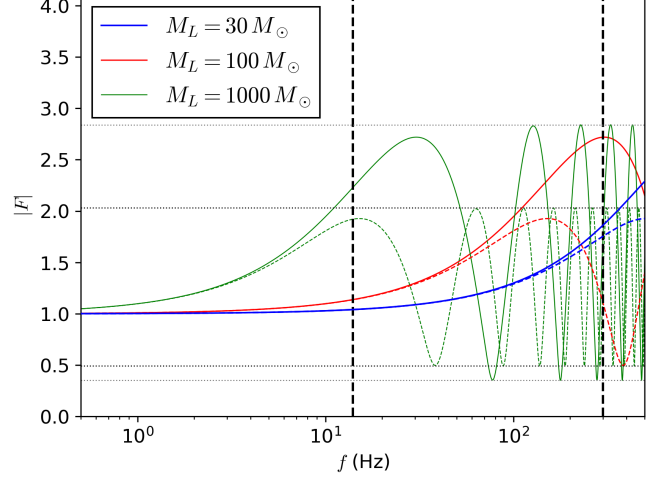


FIG. 1: Transmission factor as a function of frequency for different values of M_L at two fixed values of y : $y = 0.25$ (solid curves) and $y = 0.5$ (dashed curves).

The black vertical dashed lines correspond to $f = 15 \text{ Hz}$, given by the sensitivity of the detector, and $f = 300 \text{ Hz}$, the merger frequency for a $M_{det} = M_1 + M_2 = 60 M_\odot$ BH binary.

For calculations that are numerically expensive we use a hybrid transmission factor function that takes the value of the full-wave F from Eq. (2) at low frequencies and its GO limit given by Eq. (8) at high frequencies. The simplicity of the GO formula makes the computation much faster. As a matching point between these solutions, we take the frequency of the third oscillation maximum to ensure a smooth transition.

B. SNR increase

The detectability of a GW signal may be characterized by the signal-to-noise ratio (SNR). Within the matched filtering analysis, it is calculated as a noise-weighted inner product of the frequency-domain waveform [63, 64]

$$\rho^2 = \langle h, h \rangle = 4 \int_{f_{\min}}^{f_{\max}} \frac{|\tilde{h}(f)|^2}{S_n(f)} df, \quad (12)$$

from the minimum frequency of the detector f_{\min} to the maximum one f_{\max} , where $S_n(f)$ is the one-sided noise power spectral density of the detector. The relative SNR increase due to lensing can then be written as the ratio

between the lensed and unlensed SNRs:

$$\rho_{\text{rel}}^2 = \frac{\langle h, h \rangle}{\langle h_{UL}, h_{UL} \rangle}. \quad (13)$$

We will primarily consider gravitational waves from binary black hole coalescence since they are the most massive, the furthest away from the detector, and thus the most likely to be lensed. The typical waveform starts as a binary inspiral, which has an amplitude proportional to $f^{-7/6}$ until the merger frequency which is inversely proportional to the total mass of the binary [63].

We consider gravitational wave strain amplitudes obtained with LVK’s IMRPhenomD waveform [65, 66] that go through the standard inspiral, merger and ringdown phases. The effect of lensing on the SNR increase is demonstrated in Fig. 2. We take the usual $M_{\text{det}} =$

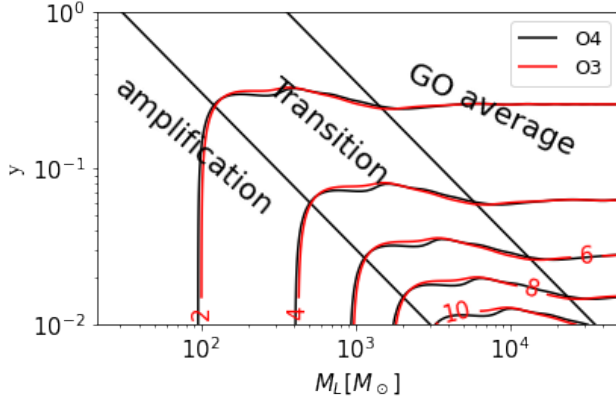


FIG. 2: Relative increase in signal-to-noise ratio ρ_{rel} as a function of y and M_L for the same black hole binary of $M_{\text{det}} = M_1 + M_2 = 60 M_\odot$ for the O3 and O4 LIGO power spectra densities. The oblique black lines delimit the regions where the amplification and the GO approximations are valid, and the transition between them.

$M_1 + M_2 = 60 M_\odot$ binary and represent the results in terms of two lensing parameters, M_L and y . Since it is a ratio, ρ_{rel} is roughly independent of the LVK noise curve used showing very similar results for O3 and O4. The characteristic behavior in different regions can be understood by comparing with the transmission factor represented in Fig. 3. At low frequency there is only amplification, following the asymptote [Eq. (7)], the dashed blue line. In the amplification-only region, and for the “close alignment” condition, the SNR increase will depend only on M_L :

$$\rho_{\text{rel}}^2 = 2\pi^2 t_M \frac{K_1}{\rho_{UL}} \propto M_L, \quad (14)$$

where $K_1 = \langle f h_{UL}, h_{UL} \rangle$ and $\rho_{UL} = \langle h_{UL}, h_{UL} \rangle$ can be seen as moments of the detector sensitivity, which are both independent of the lens parameters.

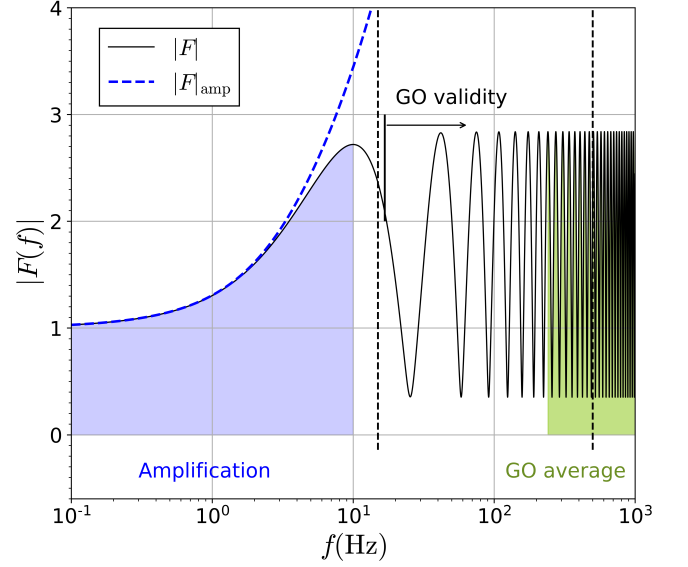


FIG. 3: Transmission factor $|F|$ as a function of frequency f , for fixed values of $M_L = 3000 M_\odot$ and $y = 0.25$. The LVK detectability lies between the black dashed lines with a maximum $f = 500$ Hz for illustrative purposes. There are two colored regions of interest related to the SNR increase shown in Fig. 2: (i) the amplification region [Eq. (7)] and (ii) the GO average region [Eq. (15)].

For higher frequencies, oscillations appear due to interference between two images of the source, in the GO limit. Since the SNR integrates over the frequencies, the oscillations in Eq. (8) tend to cancel out. When the number of oscillations is sufficient (approximately from the 8th maximum, the green region in Fig. 3), well beyond the onset of the oscillations, they asymptotically average out to

$$\langle |F|_{\text{GO}} \rangle \approx \sqrt{\frac{y^2 + 2}{y\sqrt{y^2 + 4}}} \quad (15)$$

which is independent on f and M_L . Thus, in this “GO average” region, the SNR increase depends only on y , as seen in Fig. 2:

$$\rho_{\text{rel}}^2 = \frac{y^2 + 2}{y\sqrt{y^2 + 4}} \approx \frac{1}{y}, \quad (16)$$

where the last approximation is valid for the “close alignment” condition.

III. WAVEFORM MISMATCH: MATCHING LENSED EVENTS TO EXISTENT TEMPLATES

Microlensing is not just an overall amplification of the signal, but a frequency-dependent change to the amplitude and phase of the gravitational wave. This intrinsic

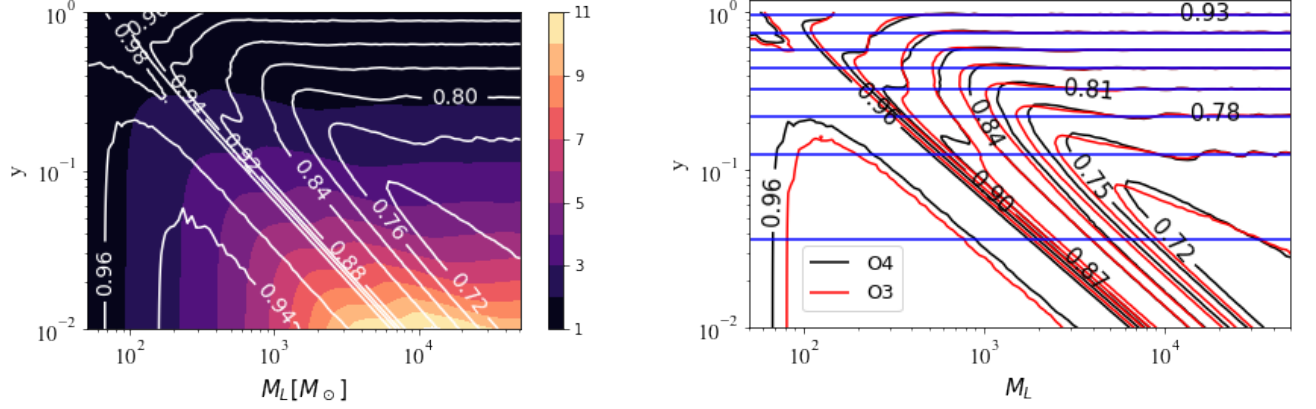


FIG. 4: Match between a lensed and unlensed waveform from a $M_{det} = 60M_\odot$ black hole binary (a) superimposed on the SNR increase computed for O4 (b) for O3 and O4 power spectra densities. It can be seen that the highest mismatch occurs for high SNR increase. The solid blue lines is the match computed in the GO limit from Eq. (20), which agrees for higher M_L and y . The change from O4 to O3 has minor effects.

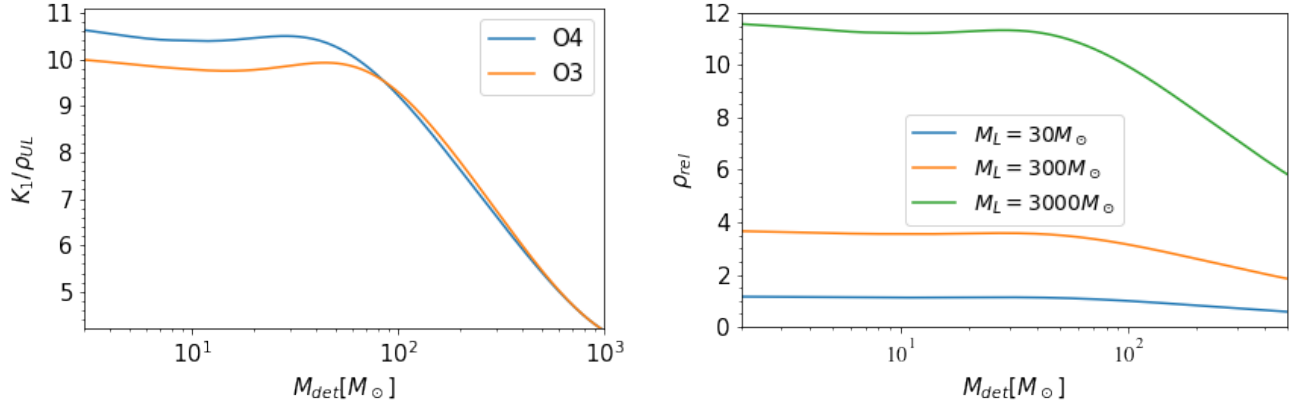


FIG. 5: (a) First SNR moment K_1 relative to the unlensed ρ for O3 and O4 power spectra densities (b) ρ_{rel} in the amplification region as a function of total mass $M_{det} = M_1 + M_2$.

distortion of the signal is what will provide our evidence of lensing. The degree of similarity between two waveforms is quantified by the match, which ranges from zero to one. The match is the overlap defined below maximized over phase and time, as this is what the detection process will do. The detectability of a given lens is computed by finding the optimal match between the lensed waveform and unlensed waveforms in the LVK's template bank. The SNR of a detection made with the unlensed template bank will be reduced proportionally to the match. In what follows, we will also use the mismatch, defined as one minus the match.

We start by determining the overlap between the lensed waveform and its unlensed counterpart, which is defined as

$$\mathcal{O}(h, h_{UL}) = \frac{\langle h, h_{UL} \rangle}{\sqrt{\langle h_{UL}, h_{UL} \rangle \langle h, h \rangle}} \quad (17)$$

The denominator can be written in terms of the SNR:

$$\mathcal{O}(h, h_{UL}) = \frac{\langle h, h_{UL} \rangle}{\rho_{UL} \rho} \quad (18)$$

In the amplification region, the overlap simplifies to

$$\begin{aligned} \mathcal{O}(h, h_{UL}) &= \frac{\langle f^{1/2} h_{UL}, h_{UL} \rangle}{\rho_{UL} \sqrt{\langle f h_{UL}, h_{UL} \rangle}} \\ &= \frac{K_{1/2}}{\rho_{UL} \sqrt{K_1}}, \end{aligned} \quad (19)$$

where $K_{1/2} = \langle f^{1/2} h_{UL}, h_{UL} \rangle$ and $K_1 = \langle f h_{UL}, h_{UL} \rangle$ are constant relative to the lens parameters. Thus in this regime the overlap is independent of y and M_L . Further, note that Eq. (19) is a lower bound for the match. When optimization over phase and time is performed, it can result in higher overlap.

In the GO average region, two images $h = h_1 + h_2$ begin to appear, separated by a time delay. Because of

the time delay, the unlensed template can only align with one of the two images, so the match is determined by the magnitude of the first (stronger) image relative to the sum of the magnitude of both images

$$\mathcal{M}_{\text{matchGO}}(h, h_{UL}) = \frac{\max_{\varphi, t} \langle h, h_{UL} \rangle}{SNR_{UL} \sqrt{\mu_1 + \mu_2}} \quad (20)$$

$$= \frac{\sqrt{\mu_1}}{\sqrt{\mu_1 + \mu_2}},$$

with the magnification of each of the images being

$$\mu_{1,2} = \frac{1}{4} \left(\frac{y}{\sqrt{y^2 + 4}} + \frac{\sqrt{y^2 + 4}}{y} \pm 2 \right). \quad (21)$$

Fig. 4 shows the match between an unlensed and a lensed equal mass $M_{\text{det}} = 60 M_\odot$ black hole binary. We use the LVK's standard IMRPhenomD templates with no spin, precession or eccentricity included. Preliminary results that included optimization over mass and spin showed a difference of under 1 %. We so far find that the optimal match occurs between the lensed h and unlensed waveform h_{UL} of the same binary mass. However, a more exhaustive parameter study is needed. In Fig. 4(a) we place the increase in SNR and the match on the same plot in $y - M_L$ space. The two regions: amplification (left corner) and GO (right corner) can clearly be distinguished.

If the source has $\rho \approx 10$, a mismatch higher than 20% can bring it just under the detectability threshold $\rho = 8$, rendering it undetectable. As we will see in the next section, sources with lower 'actual' ρ are more likely to be lensed because they are expected to be further away. As per the figure, a distant source of $\rho_{UL} = 1$ could increase its SNR by a factor of 10 and appear detectable at $\rho = 8$ with a match of 84%.

Fig. 4(b) compares the optimal match computed for the same $M_{\text{det}} = 60 M_\odot$ binary for O3 and predicted O4 noise curves. As shown mathematically, in the geometrical optics region both the match and SNR increase are insensitive to the noise curve used. They only depend on the distance from the line of sight y . In the silent amplification region, where the match is generally over 90%, some difference is observed due to variations in the first SNR moment K_1 (see Fig. 5(a) and (b) for K_1/ρ_{UL} and ρ_{rel}). Minor variations in the match are also observed in the region where the full transmission factor is required for the calculation. The vertical blue line shows the analytic formula given by Eq. (20) from the GO estimate. The oblique line corresponds to points in $y - M_L$ phase space where the amplification and the GO regions meet.

IV. THE IMPRINT OF THE LENS ON THE GRAVITATIONAL WAVE STRAIN

The transmission factor imprints the gravitational lensing effect on the original waveform $\tilde{h}_{UL}(f)$, as

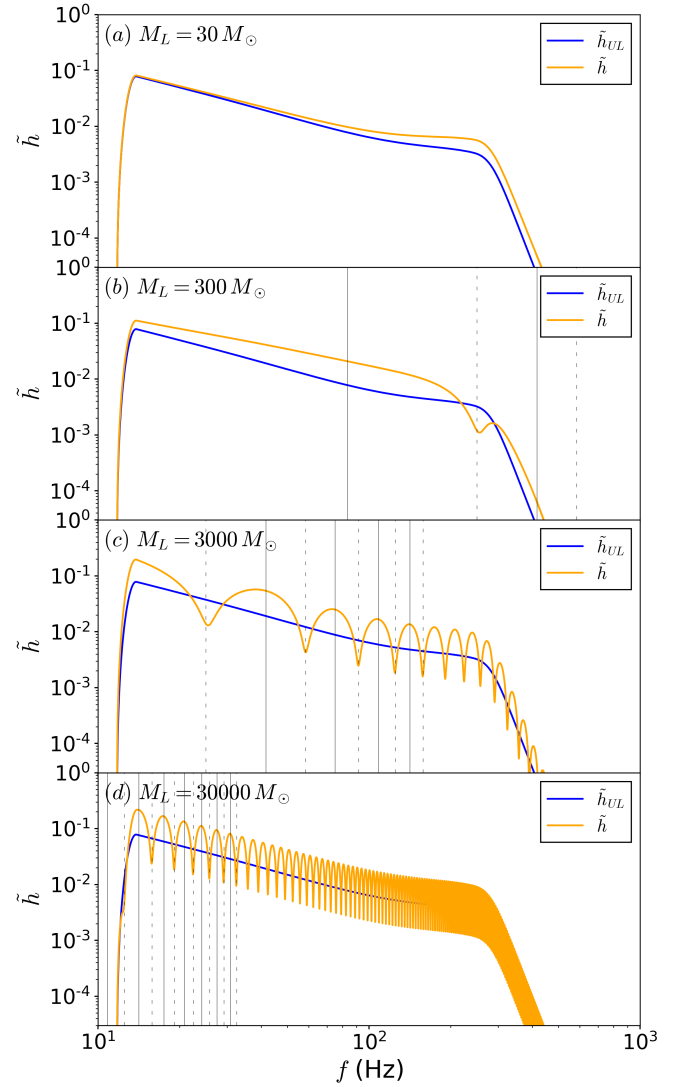


FIG. 6: Frequency domain strain of a lensed gravitational wave (in orange) compared to the unlensed one (in blue), as a function of frequency for $y = 0.25$.

The effects of lensing are seen as amplification and modulation (beating pattern, due to the interference between images). The predicted locations of the maxima and minima are shown with vertical lines. It can be seen they correspond to maxima and minima of the waveform (dashed and solid lines respectively).

$\tilde{h}(f) = \tilde{h}_{UL}(f)F(f)$. In this section we will show its effect, both in the frequency domain as $\tilde{h}(f)$ and its Fourier transform $h(t)$, the strain in time domain. We consider the $M_{\text{det}} = 60 M_\odot$ gravitational waveform used in Sec. II.

Fig. 6 compares the lensed $|\tilde{h}(f)|$ with the unlensed $|\tilde{h}_{UL}(f)|$ waveforms, when the position of the lens is fixed at $y = 0.25$. The mass of the lens changes from $M_L = 30 M_\odot$ to $M_L = 30000 M_\odot$. The two behaviours of the transmission factor can also be seen here in the imprint:

- (i) When M_L is small (i.e. for $y = 0.25$, $M_L = 30 M_\odot$)

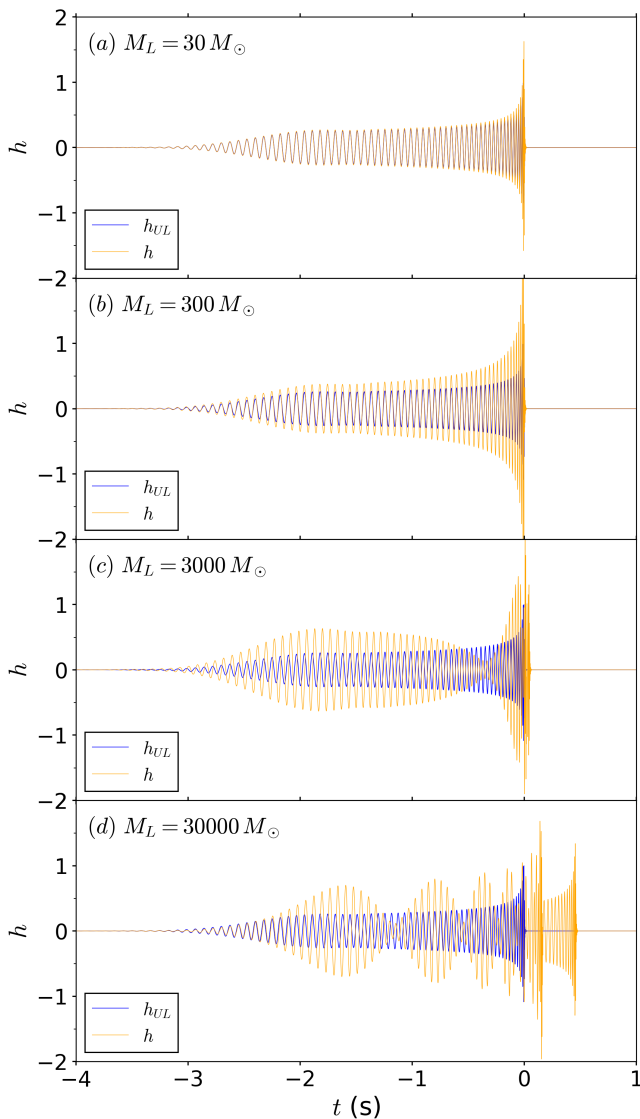


FIG. 7: Time domain strain of a lensed gravitational wave (in orange) compared to the unlensed one (in blue), as a function of time for $y = 0.25$. The lensing effects are seen as amplification and modulation (beating pattern). When two images appear (d), both the first and the second lensed images can be seen arriving later than the unlensed one. Unlike other processes that can cause beating patterns, the presence of two separate images is a unique feature of gravitational lensing.

in Fig. 1 and Fig. 6(a)), the transmission factor $|F|$ is a monotonic function: the amplification of the signal is gradually increasing with frequency. The highest magnification occurs at merger (the frequency is highest there).

(ii) For higher lens mass, $|F|$ has oscillations at high enough frequencies (from the first maximum at $f_1^+ = 1/(8t_M y) \approx 2.5 \cdot 10^4 M_\odot/M_L$). The positions of con-

structive and destructive interference can be deduced using Eq. (9). These are imprinted on the strain as seen in Fig. 6(b),(c),(d), and are depicted with vertical solid and dashed lines respectively. As seen in Sec. II, the fringe spacing Δf is dependent on the product $y t_M$, while the amplitude of the oscillations only depends on y .

The time evolution of the lensed gravitational wave strain, $h(t)$, is obtained by taking the Fourier transform of $\tilde{h}(f)$. The results are shown in Fig. 7 again at fixed $y = 0.25$, while M_L varies. For small mass like $M_L = 30 M_\odot$, the lensed waveform is just amplified relative to the unlensed one. The amplification is monotonic for $|F|$ and thus largest for the frequencies close to the merger. For higher M_L , a “beating pattern” (amplitude modulation) appears, caused by the interference between the two images. The beating frequency increases with frequency [28]. In Fig. 7(d) we can see two separate images appearing, each one coming with a different time delay with respect to the unlensed case. The earliest signal is the interference between the two images (containing the beating pattern), followed by the the first image of the merger. Afterwards, the second image arrives alone without interference, therefore having the shape of a single chirp (but affected by magnification). Both images have different magnifications respect to the unlensed signal, which are dependent on y [Eq. (21)]. Unlike the amplification and beating pattern, which can be mimicked by other processes (precession [60, 61], eccentricity [62]), the detection of the two separated images is a unique and distinct feature of gravitational lensing.

Another representation of the detected signal is a spectrogram that shows the signal-power in the time-frequency plane. The signal is characterized by a dimensionless quality factor Q :

$$Q = \frac{f_c}{\sigma_f}, \quad (22)$$

where f_c and σ_f are the central frequency, and bandwidth of the signal in frequency space. In this work we are using the Q-transform package provided by LVK’s pyCBC software to compute the Q-transformed strain.

Fig. 8 shows the signal power in white noise for fixed $y = 0.25$ and increasing M_L . For $M_L = 30 M_\odot$ the signal looks like an unlensed signal, but in reality it is brighter than its unlensed counterpart at high frequencies, due to the amplification effect. For higher lens mass (Fig. 8(c), (d) and (e)), the two images –marked as 1, 2 in the figure– separate at high frequencies. For these same subfigures, at low frequencies we observe distortions resembling a crab’s claw: the appearance of dim regions where the signal is suppressed (“holes”) and of bright regions where the signal is stronger. These correspond to destructive interference (minima) and constructive interference (maxima), represented by white dashed and solid lines respectively, as predicted by Eq. (9). The separation between two consecutive maxima/minima is given by $\Delta f = 1/(2y t_M)$ in the “close alignment” regime [Eq. (10)]. As M_L increases, so does the number of bright

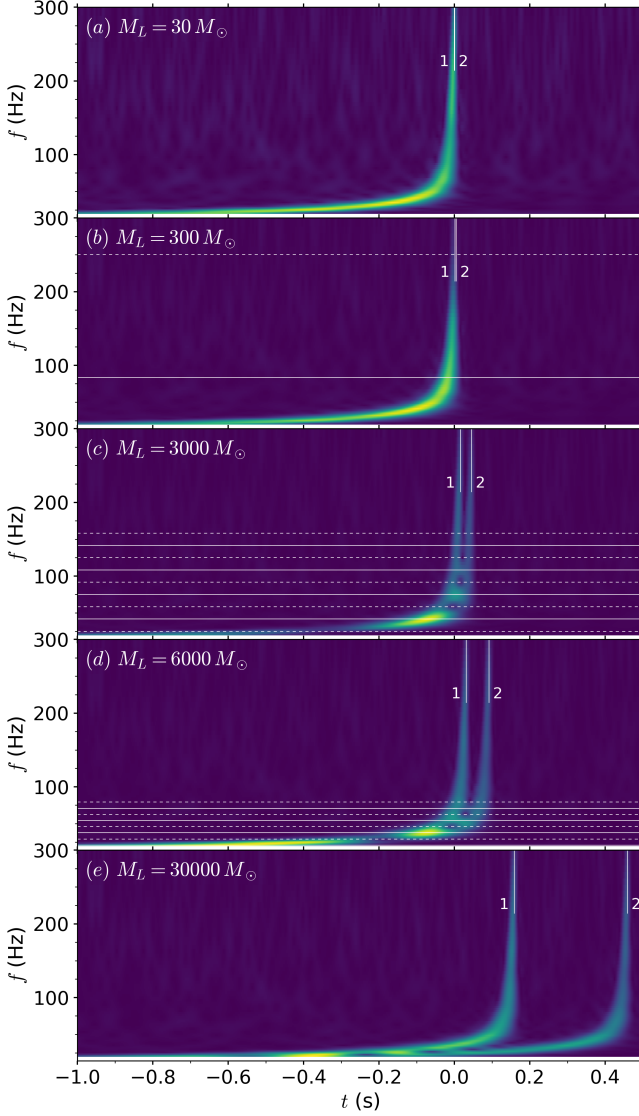


FIG. 8: Spectrograms of the lensed signal for $y = 0.25$, and increasing M_L in white noise. In (a), the signal is amplified by a monotonic $|F|$. As M_L increases, the interference pattern first appears at higher frequencies (for lower M_L , subplots (b) and (c)) and at lower frequencies for higher M_L (subplots (d) and (e)). The estimated frequencies for constructive interference (maxima) and destructive interference (minima) given by Eq. (9) are marked in white solid and dashed lines respectively, in subplots (b), (c), (d). The two images of the merger (1 and 2) are marked with white vertical lines. Their separation Δt_{21} increases with the product $y t_M \propto y M_L$.

regions and holes. For higher masses they progressively appear at lower frequencies.

The separation between the images increases with mass. Both GO images are delayed in time with respect to the unlensed signal, whose merger peak would be at

Model	$M_L [M_\odot]$	match	SNR Increase (ρ_{rel})
1a	30	98.5%	1.3
1b	300	92.8 %	2.1
1c	3000	78.4%	2.0
1d	6000	78.9 %	2.0

TABLE I: Model parameters for lensed signals with $y = 0.25$ in simulated O4 noise. Increasing M_L will not alter the match or ρ_{rel} further since the system has reached the GO average, where the match and SNR increase only depend on y .

$t = 0$. Their positions can be predicted: the position of the first image is obtained as the minimum of the Fermat potential (see e.g. [7] for more details),

$$t_1 = \left[\frac{1}{2}(x_1 - y)^2 - \ln |x_1| \right] t_M \quad (23)$$

where $x_1 \equiv (1/2)(y + \sqrt{y^2 + 4})$ corresponds to the dimensionless spatial position of the first image in the lens plane. The time delay of the second image is obtained by adding Δt_{21} to t_1 (Δt_{21} is also analytic, see e.g. [7, 36]).

This time delay between the images is inversely proportional to the separation between two maxima/minima in frequency: $\Delta t_{21} = 1/\Delta f$. Therefore, if detectors found multiple maxima/minima (obtaining their separation Δf) and the time delay Δt_{12} , by comparing them one could confirm or reject the lensing nature of the signal. The time delay can therefore be obtained through two separate measurements: (i) separation of GO images in time Δt_{21} , directly in $h(t)$ and $f(t)$, and (ii) through the fringe spacing in frequency, $\Delta t_{21} = 1/\Delta f$. If these two measurements coincided, it would confirm a detection of lensing, and reject “mimickers” – other astrophysical effects that produce multiple chirps and beating patterns similar to lensing.

Most signals will be detected at SNRs close to the threshold SNR. Then, in practice, the minima and maxima might not be observable by eye due to the abundance of noise. Fig. 9 shows spectrograms in simulated O4 noise at signal to noise $\rho = 10$ for $y = 0.25$ and several values of M_L between $30M_\odot$ and $6000M_\odot$. It can be seen that some maxima and minima are visible, but the whole waveform becomes difficult to distinguish. Table I shows the match and SNR increase for Model 1a–d. Beyond $M_L = 3000M_\odot$, ρ_{rel} and the mismatch stop growing since lensing is independent of M_L once the GO average is reached. An injection of higher SNR will leave Table I unchanged. At $\rho \geq 20$, the spectrograms will look similar to those in Fig. 8. A manuscript that focuses on detectability and parameter recovery in each region (amplification, transition, GO) is currently in preparation.

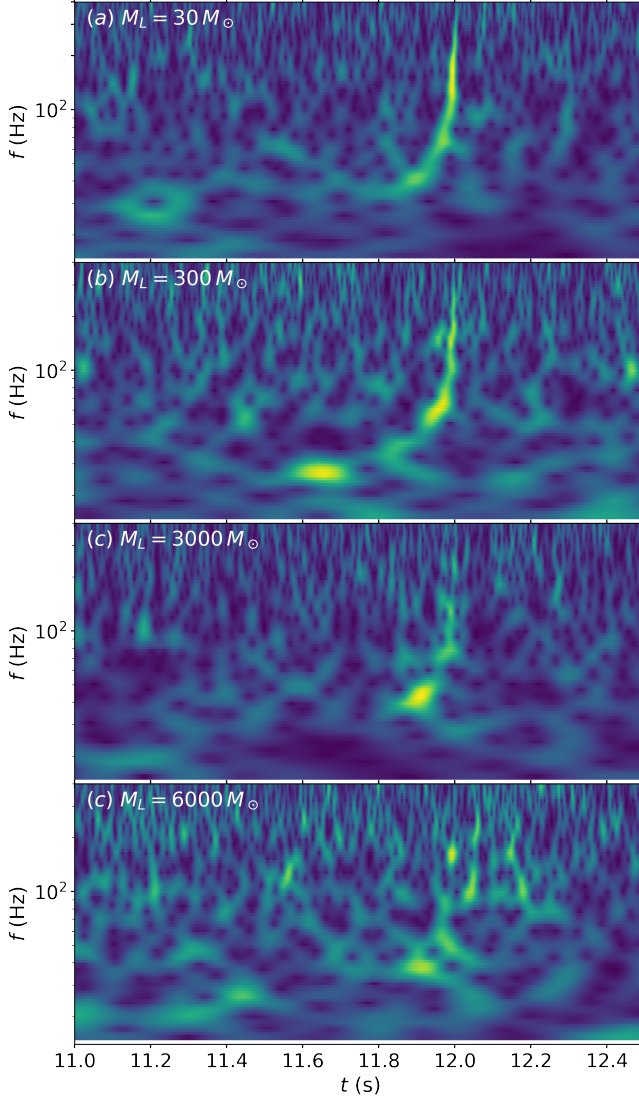


FIG. 9: Spectrograms of the lensed signal in simulated O4 noise at $\rho = 10$ for $y = 0.25$ and M_L varying between $30M_\odot$ and $6000M_\odot$.

V. PROBABILITY OF DETECTION: AN UPPER LIMIT

The distribution of lenses in angle is scale-free for lenses sufficiently near the line of sight, i.e., independent of M_L . The lensing angles are distributed uniformly in area, as $y dy$. This uniform prior distribution over y is currently used when performing parameter estimation of possibly lensed signals. Our approach is to estimate lens parameters only for the events which are detectable by the gravitational-wave search. This causes a strong selection bias for smaller values of y because they lead to substantial magnification. The magnification increases the volume containing sources, as well as the probability of encountering a lens due to the greater distance. Thus the prior on y is enhanced toward smaller values when

selecting for detected events. Our derivation will follow the lines of [67] (and see [48] for an application to gravitational waves), but adding the effect of selection bias due to detectability above an SNR threshold.

The probability that a given detection is lensed is given by the relative rates of lensed and unlensed detections,

$$P_{\text{lensing}}(M_L, n_L) = \frac{N_{LS}}{N_S}, \quad (24)$$

where N_{LS} is the number of lensed sources above the threshold SNR ρ_t , and likewise N_S is the number of unlensed detectable sources. We will consider below a few different criteria for a source to be meaningfully lensed. Observe that this relative probability is independent of any overall scaling of the number density of sources, which we will denote n_S .

To incorporate cosmology, we will write our integrals in terms of the radial comoving distance

$$\chi = \int \frac{dz'}{H(z')} \quad (25)$$

where $H(z)$ is the Hubble parameter. We assume standard cosmology

$$H(z) = H_0 \sqrt{\Omega_M(1+z)^3 + \Omega_\Lambda}, \quad (26)$$

with $H_0 = 69.6 \text{ km s}^{-1} \text{ Mpc}^{-1}$, $\Omega_M = 0.286$, $\Omega_\Lambda = 0.714$. As the universe is spatially flat, the transverse and radial comoving distances are identical. The volume integrand is simply $dV = \chi^2 d\chi d\Omega$.

The total number of sources with SNR above a detection threshold ρ_t can be written as

$$N_S = 4\pi \int_0^{\chi_t} n_S \chi_S^2 d\chi_S = \frac{4\pi}{3} \chi_t^3 n_S. \quad (27)$$

Above, χ_t is the comoving distance at which the lensed source would have SNR above a threshold, which in this manuscript is $\rho_t = 10$. For simplicity, we are assuming that the comoving number density of lenses n_S is independent of redshift, and also of source mass when we are considering detections where the observed mass (in the detector frame) is fixed. These effects can be included, though we note that the scenarios we consider do not extend past $z_S \approx 4$, where the density would be expected to drop. In general, constant comoving density for both sources and lenses is appropriate for e.g. primordial black holes in the absence of mergers.

We next compute the number of lensed objects N_{LS} above a threshold ρ_t as a function of source redshift z_S and lens parameters y and M_L . This involves an integral over both the lens and source location

$$N_{LS} = \int n_S \int n_L dV_L dV_S. \quad (28)$$

Here n_L is the number density of lenses in a comoving volume, and we have

$$n_L dV_L = 2\pi n_L \chi_L^2 \sin \theta_L d\theta_L d\chi_L. \quad (29)$$

The angle θ_L will be very small, so that $\sin \theta_L \approx \theta_L$. This is related to the Einstein angle by $\theta_L = \theta_E y$ (see Sec. II).

The angular diameter distances can be expressed in terms of χ as $d_S = \chi_S/(1+z_S)$ and $d_L = \chi_L/(1+z_L)$. The distance from lens to source is [48]

$$d_{LS} = d_S - \frac{1+z_L}{1+z_S} d_L = \frac{\chi_S - \chi_L}{1+z_S}. \quad (30)$$

We now change variables from θ_L to y to obtain

$$N_L = 8\pi \int n_L \int M_L \frac{d_{LS}}{d_L d_S} y dy \chi_L^2 d\chi_L \quad (31)$$

$$= 8\pi \int n_L M_L \frac{(1+z_L)(\chi_S - \chi_L)\chi_L}{\chi_S} y dy d\chi_L \quad (32)$$

The integrand can be seen as a differential form of the standard lensing cross section.

Integrating over all detectable sources yields the total number of lensed sources

$$N_{LS} = 4\pi \int n_S N_L \chi_S^2 d\chi_S \quad (33)$$

$$= 32\pi^2 \int_0^{y_{\max}} dy \int_0^{\chi_t(y)} d\chi_S \int_0^{\chi_S} d\chi_L n_S \times n_L M_L (1+z_L) \chi_L (\chi_S - \chi_L) \chi_S y. \quad (34)$$

The constraint $\chi_L < \chi_S$ appears because the lens must not be beyond the source.

Importantly, the amount of lensing changes the distance to which we can observe a source. The relative SNR increase is a function of y and the redshifted lens mass $(1+z_L)M_L$. In addition to the value of this integral, we will also examine the integrand as a function of y to determine the distribution of y among systems with detectable lensing. Regions of parameter space with more lensing amplification will give larger contributions to the integral. The integrand can be used to determine the distribution of detectable sources as a function of y .

We perform our integrals by grid integration over χ_S , χ_L , and $\log y$; a Monte Carlo approach would be required if we considered more variables. We take $y_{\max} = 2$, which goes beyond the point where the lensing contribution is significant.

To parameterize the number of lenses, we take $n_L M_L = \rho_{\text{cr}}^{DM}$, which provides a strict upper limit for the lenses of a given mass. This means the probability that a certain detected black hole binary system is lensed can be lower than the numbers in this manuscript, but it cannot be higher unless the model changes e.g., the point mass lens is embedded into a larger object that can increase the lensing. The probability is independent of n_S unless it evolves significantly in the relevant redshift range.

The gravitational waves the LVK measures are at the location of the detector. In the detector frame,

$$h \propto \frac{(\mathcal{M}_{\text{det}})^{5/6}}{D_{\text{lum}}} = \frac{(\mathcal{M}_{\text{det}})^{5/6}}{(1+z_S)\chi_S}, \quad (35)$$

where the measured Chirp mass for the binary is $\mathcal{M}_{\text{det}} = (1+z_S)\mathcal{M}_{\text{src}}$.

In the source frame, the gravitational waveform from a binary inspiral is proportional to

$$h \propto \frac{((1+z_S)\mathcal{M}_{\text{src}})^{5/6}}{D_{\text{lum}}} = \frac{((1+z_S)\mathcal{M}_{\text{src}})^{5/6}}{(1+z_S)\chi_S}, \quad (36)$$

where \mathcal{M}_{src} is the Chirp mass measured at the source.

Fig. 10 displays the probability density for lensing normalized by the density of unlensed sources in the $y - M_L$ plane for several detected masses. As expected, more massive detections have a higher probability of being lensed. Figs. 10(a) and (b) show two comparable regions of mismatch 5% or higher for black hole binary systems of total detected mass $M_{\text{det}} = 30M_\odot$ and $M_{\text{det}} = 60M_\odot$. The higher y region occurs when Geometrical Optics is valid, and the lower y region corresponds to the amplification only region. As the total mass of the binary increases to $M_{\text{det}} = 120M_\odot$ (Fig. 10(c)), only the GO region is discernible reducing the $y - M_L$ range of identifiable lensed systems to a small area in the upper right corner of the plane.

Fig. 11 plots the probability density for a given lens mass $M_L = 300M_\odot$ as a function of y and source redshift z_S . Like before Figs. 11(b) and (c) (second plot on each line) shows the two separate regions for a mismatch of 5% or higher. Higher M_{det} reaches higher source redshift. For $M_{\text{det}} = 120M_\odot$ (Fig. 11(c)), potential lensed sources go up to $z_S \approx 3.2$. Unfortunately, the higher redshift systems have low mismatch and cannot be identified as lensed. For the standard $M_{\text{det}} = 60M_\odot$ (Fig. 11(b)), the highest $z_S \approx 2$ corresponds to the amplification only region. At this redshift $M_{\text{det}} = 60M_\odot$ results in a source mass of $M_{\text{det}} = 20M_\odot$ or $M_1 = M_2 = 10M_\odot$, which is closer in mass to the black holes observed in our galaxy with electromagnetic observations. The probability of lensing for such an event would be around 3% if all dark matter was composed of black holes of $M_L = 300M_\odot$.

The integrated probability density is displayed in Fig. 12 as a function of lens mass M_L for detected total binary masses ranging from $M_{\text{det}} = 30M_\odot$ to $M_{\text{det}} = 240M_\odot$ with $\rho \geq 10$. It is normalized by the total number of sources with an $\rho \geq 10$. Fig. 12(a) shows the probability for all lensed sources. We can see it peaks at low lens mass, and that the peak shifts to slightly higher masses as M_{det} increases reaching $M_L \approx 40M_\odot$ for $M_{\text{det}} = 240M_\odot$, and then flattens out as the lens mass continues to increase. In Figs. 12(a) and (b) we limit the detected black hole binaries to those whose waveform has a mismatch of $\geq 5\%$ and $\geq 10\%$, respectively. This decreases the probability of lensing to a value that is well below its peak. It can be seen that detectable lensing starts at larger values of $M_L > 100M_\odot$ and flatten out as M_L increases. For a detectable mismatch of $\geq 10\%$, increasing the detected mass from $M_{\text{det}} = 30M_\odot$ to $M_{\text{det}} = 60M_\odot$ increases the probability of detectable lensing by about a factor of 2. However, as the detectable mass increases

further, the increase in probability is less significant. Already the $M_{det} = 240M_{\odot}$ case contains lower probability events than $M_{det} = 120M_{\odot}$.

VI. CONCLUSIONS AND FUTURE DIRECTIONS

To date, the LVK collaboration has detected over 90 compact binary systems. The detectors' sensitivity can be expected to improve over the coming years. So far it appears that the black hole population seen by the LVK is an order of magnitude heavier than black holes found by Xray surveys of the Milky Way. It is known that a population could appear more massive and less distant if redshift is underestimated. Such a binary black hole population could then provide first indirect evidence of gravitational lensing.

Many sources will be lensed, which complicates parameter estimation. However, if the lens mass is low, it will not affect the waveform in a visible manner. Similarly, if the lens is far from the line of sight it will not affect the signal. We find that events that are likely to produce detectable evidence of lensing will be in the transition region reaching moderate values for y and high enough values for M_L .

We use the point-mass lens model to estimate the detectability of lensed binary black hole events by a gravitational wave detector. In this simplest model for microlensing, the lensed waveform in the frequency domain is obtained by multiplying the unlensed waveform by a transmission factor. In general, the transmission factor depends on the mass of the lens M_L and on the distance from the line of sight y between the source and the observer. Lensing induces (1) frequency dependent amplification and (2) distortion of the waveform arising from constructive and destructive interference between two virtual images of the source. If diffraction dominates, only the frequency dependent amplification occurs, which solely depends on M_L . Conversely, when two virtual images of the source interfere, the geometrical optics limit assures that the transmission factor depends only on y . Gravitational lensing then introduces a regular beating pattern (areas of constructive and destructive interference) that is predicted analytically.

We map the SNR increase as a function of lens parameters y and M_L . To estimate detectability, we produce a map of the optimal match between the lensed waveform and its unlensed counterparts, while optimizing over the amplitude and phase of the gravitational wave. A mismatch of 10% is assumed to be confidently detectable. While a mismatch of 5% results is considered to be mild evidence for lensing.

Most importantly, we show that the mismatch causes a selection bias with a prior on the distance from the line of sight y that is enhanced toward smaller values of y when selecting events. We find that it is misleading to assume the lensing angles are distributed uniformly in

area as ydy , and that future LVK searches should include this non-trivial prior.

This paper incorporates the requirement that the lensing not only amplify the signal, but also leave a detectable imprint that confirms the existence of the microlense. This is only a fraction of the parameter space; otherwise we have 'silent' lensing. In that case the distance to the binary and the mass of the binary could be affected by lensing without creating a detectable mismatch with unlensed templates. Because the lensing does not affect these waveforms, the likelihood of the lensed and unlensed signals will be identical, and the Bayesian evidence ratio would only reflect the relative volume of the priors. In this first study we do not include a specific model that predicts the number and masses of lenses since they are so uncertain. We leave that to future work. Instead we show the priors when they are conditioned as well on the lensed waveform having a sufficient mismatch that it leaves a measurable imprint on the signal.

Ultimately, we find that lensing can bias the redshift distribution and that most lensed sources have low mismatch (mismatch $< 5\%$) that cannot be detected. Furthermore, when including all lensed sources, we do not reach a redshift beyond 4 with LVK detectors. Mild evidence for lensing (mismatch of 5% or higher) can be obtained up to $z = 2$ for more massive detections $M_{det} = 120$, which in the source frame would be consistent with a total binary mass $M_{src} = M_1 + M_2 = 40M_{\odot}$.

We find that compact lenses (e.g., primordial black holes) of $M_L = 30M_{\odot}$ in the LVK band provide only slight amplification of the gravitational signal of about 20% without distortion. We conclude that in the point mass lens approximation, lenses of $20-30M_{\odot}$ have a minimal effect on the detected mass of binary black holes unless they can be embedded in heavier dark matter structures. More work is needed to go beyond the point mass lens model.

In this paper we have taken the critical density of dark matter as a reference and upper limit for the number density of lenses $n_L m_L < \rho_{cr}^{DM}$. We note that this manuscript takes the co-moving density to be constant for both the sources and the lenses, which is a simplified assumption that is valid only when the number of mergers is negligible. We will relax this assumption and consider more realistic distributions in future work.

ACKNOWLEDGEMENTS

The authors are grateful to the members of the Gravitational Waves research group from ICC UB for their continual advice and support. We particularly thank Mark Gieles, Tomas Andrade, Juan Trenado, and Daniel M. Pina. We also thank ICC secretaries, Esther Pallarés Guimerà and Anna Argudo who go well beyond their job to keep everything running smoothly.

We acknowledge support from the Spanish Ministry of Science and Innovation through grant PID2021-

125485NB-C22 and CEX2019-000918-M funded by MCIN/AEI/10.13039/501100011033. AL is supported by STFC grants ST/T000550/1 and ST/V005715/1. Supporting research data are available on reasonable re-

quest from AL. For the purpose of open access, the author(s) has applied a Creative Commons Attribution (CC BY) licence to any Author Accepted Manuscript version arising.

-
- [1] B. P. Abbott et al. (LIGO Scientific and Virgo Collaborations), Phys. Rev. Lett. **116**, 061102 (2016).
 - [2] B. P. Abbott et al. (LIGO Scientific and Virgo Collaborations), arXiv:1811.12907 (2018), Phys. Rev. X **9**, 031040 (2019).
 - [3] R. Abbott et al. (LIGO Scientific and Virgo Collaborations), arXiv:2010.14527 (2020), Phys. Rev. X **11**, 021053 (2021).
 - [4] R. Abbott et al. (LIGO Scientific and Virgo Collaborations), arXiv:2111.03606 (2021).
 - [5] J.M. Diego, O.A. Hannuksela, P.L. Kelly, T. Broadhurst, K. Kim, T.G.F. Li, and G.F. Smoot, Astron. and Astrophys. **627**, A130 (2019).
 - [6] J.M. Diego, Phys. Rev. D **101**, 123512 (2020).
 - [7] P. Schneider, J. Ehlers, and E. Falco, *Gravitational Lenses* (Springer, New York, 1992).
 - [8] A.O. Petters, H. Levine, and J. Wambsganss, *Singularity Theory and Gravitational Lensing* (Birkhauser, Boston, 2001).
 - [9] M. Sereno, A. Sesana, A. Bleuler, P. Jetzer, M. Volonteri, and M.C. Begelman, Phys. Rev. Lett. **105**, 251101 (2010).
 - [10] Ng, K. K., Wong, K. W., Broadhurst, T., and Li, T. G., Phys. Rev. D **97**, 023012 (2018).
 - [11] S.-S. Li, S. Mao, Y. Zhao, and Y. Lu, Mon. Not. R. Astron. Soc. **476**, 2220 (2018),
 - [12] M. Oguri, Mon. Not. R. Astron. Soc. **480**, 3842 (2018)
 - [13] M. Oguri, Rep. Prog. Phys. **82**, 126901 (2019).
 - [14] G.P. Smith, M. Jauzac, J. Veitch, W.M. Farr, R. Massey, and J. Richard, Mon. Not. R. Astron. Soc. **475**, 3823 (2018)
 - [15] Ryczanowski, D., Smith, G. P., Bianconi, M, et al., Mon. Not. R. Astron. Soc. **495**, 1666 (2020)
 - [16] Robertson, A., Smith, G. P., Massey, R , et al., Mon. Not. R. Astron. Soc. **495**, 3727 (2020)
 - [17] T. T. Nakamura, Phys. Rev. Lett. **80**, 1138 (1998).
 - [18] T. T. Nakamura and S. Deguchi, Progress of Theoretical Physics Supplement **133**, 137 (1999).
 - [19] R. Takahashi and T. Nakamura, Astrophys. J. **595**, 1039 (2003).
 - [20] N. Matsunaga and K. Yamamoto, JCAP **2006** 023 (2006).
 - [21] Z. Cao, L.-F. Li, and Y. Wang, Phys. Rev. D **90**, 062003 (2014).
 - [22] K.-H. Lai, O.A. Hannuksela, A. Herrera-Martín, J.M. Diego, T. Broadhurst, and T.G.F. Li, Phys. Rev. D **98**, 083005 (2018).
 - [23] Christian, P., Vitale, S., and Loeb, A., Phys. Rev. D **98**, 103022 (2018).
 - [24] K. Liao, M. Biesiada, and X.-L. Fan, Astrophys. J. **875**, 139 (2019).
 - [25] S. Hou, X.-L. Fan, K. Liao, and Z.-H. Zhu, Phys. Rev. D **101**, 064011 (2020).
 - [26] D.J. D’Orazio and A. Loeb, Phys. Rev. D **101**, 083031 (2020).
 - [27] Cheung, M. H. Y., Gais, J., Hannuksela, O. A., and T.G.F. Li, Mon. Not. R. Astron. Soc. **503**, 3326 (2021).
 - [28] S. Hou, P. Li, H. Yu, M. Biesiada, X.-L. Fan, and Z.-H. Zhu, Phys. Rev. D **103**, 044005 (2021).
 - [29] P. Cremonese, J. M. Ezquiaga, and V. Salzano, Phys. Rev. D **104**, 023503 (2021).
 - [30] P. Cremonese, D.F. Mota, and V. Salzano, arXiv:2111.01163 (2021).
 - [31] H. Yu, Y. Wang, B. Seymour, and Y. Chen, Phys. Rev. D **104**, 103011 (2021).
 - [32] M. Biesiada and S. Harikumar, Universe, **7**, 502 (2021).
 - [33] A.K-W. Chung and T.G.F. Li, Phys. Rev. D **104**, 124060 (2021).
 - [34] A.G. Suvorov, Astrophys. J. **930**, 13 (2022).
 - [35] C. Dalang, G. Cusin and M. Lagos, Phys. Rev. D **105**, 024005 (2022).
 - [36] O. Bulashenko and H. Ubach, JCAP **2022** 022 (2022).
 - [37] J. Gais, K. Ng, E. Seo, K.W.K. Wong and T.G.F. Li, Astrophys. J. Lett. **932**, L4 (2022).
 - [38] H.G. Choi, Ch. Park, and S. Jung, Phys. Rev. D **104**, 063001 (2021).
 - [39] Z. Gao, X. Chen, Y.M. Hu, J.D. Zhang, and Sh.J. Huang, Mon. Not. R. Astron. Soc. **512**, 1 (2022).
 - [40] X. Guo and Y. Lu, Phys. Rev. D **106**, 023018 (2022).
 - [41] T. Suyama, T. Tanaka, and R. Takahashi, Phys. Rev. D **73**, 024026 (2006).
 - [42] I. Fernández-Núñez and O. Bulashenko, Phys. Lett. A **380**, 2897 (2016).
 - [43] I. Fernández-Núñez and O. Bulashenko, Phys. Lett. A **381**, 1764 (2017).
 - [44] S. Jung and C. S. Shin, Phys. Rev. Lett. **122**, 041103 (2019).
 - [45] B. Liu, Z. Li, and Z.-H. Zhu, Mon. Not. R. Astron. Soc. **487**, 1980 (2019).
 - [46] K. Liao, Sh. Tian, and X. Ding, Mon. Not. R. Astron. Soc. **495**, 2002 (2020).
 - [47] J.S. Wang, A. Herrera-Martín, and Y.M. Hu, Phys. Rev. D **104**, 083515 (2021).
 - [48] J. Urrutia and V. Vaskonen, Mon. Not. R. Astron. Soc. **509**, 1358 (2022).
 - [49] Basak, S., Ganguly, A., Haris, K., et al., Astrophys. J. Lett., 926, L28 (2022).
 - [50] O. A. Hannuksela, K. Haris, K.K.Y. Ng, S. Kumar, A.K. Mehta, D.Keitel, T.G.F. Li, and P. Ajith, Astrophys. J. Lett., 874, L2 (2019).
 - [51] R. Abbott et al. (LIGO Scientific and Virgo Collaborations), Astrophys. J. Lett., 923, 14 (2021).
 - [52] R. Abbott et al. (LIGO Scientific, Virgo and KAGRA Collaborations), (unpublished) (2022)
 - [53] LIGO, Virgo AND KAGRA Observing Run Plans, <https://observing.docs.ligo.org/plan/>
 - [54] *An Overview of Gravitational Waves: Theory, Sources and Detection*, edited by G. Auger and E. Plagnol (World Scientific, 2017).
 - [55] M. Maggiore, C. Van Den Broeck and N. Bartolo et al.,

- JCAP **2020** 050 (2020).
- [56] E. Barausse et al. (LISA Collaboration), Gen. Relativ. Gravit. **52**, 81 (2020).
 - [57] M. Bailes, B.K. Berger, P.R. Brady, et al., Nat. Rev. Phys **3**, 344 (2021).
 - [58] S. Deguchi and W. D. Watson, The Astrophys. J., **307**, 30 (1986).
 - [59] S. Deguchi and W. D. Watson, Phys. Rev. D **34**, 1708 (1986).
 - [60] M. Hannam, Gen. Relativ. Gravit. **46**, 1767 (2014).
 - [61] P. Schmidt, F. Ohme, and M. Hannam, Phys. Rev. D **91** 024043 (2015).
 - [62] A. Ramos-Buades, A. Buonanno M. Khalil, and S. Ossokine, Phys. Rev. D **105** 044035 (2022).
 - [63] C. Cutler and E.E. Flanagan, Phys. Rev. D **49**, 2658 (1994).
 - [64] E.E. Flanagan and S.A. Hughes, Phys. Rev. D **57**, 4535 (1998).
 - [65] S. Khan, S. Husa, M. Hannam, et *al.*, Phys. Rev. D **93**, 044007 (2016), arXiv:1508.07253.
 - [66] S. Husa, S. Khan, M. Hannam, M. Pürrer, F. Ohme, X. Jiménez Forteza, and A. Bohé, Phys. Rev. D **93**, 044006 (2016) arXiv:1508.07250.
 - [67] E. Turner, J. Ostriker, J. R. Gott III, Astrophys. J. Lett., **284**, 1 (1984).

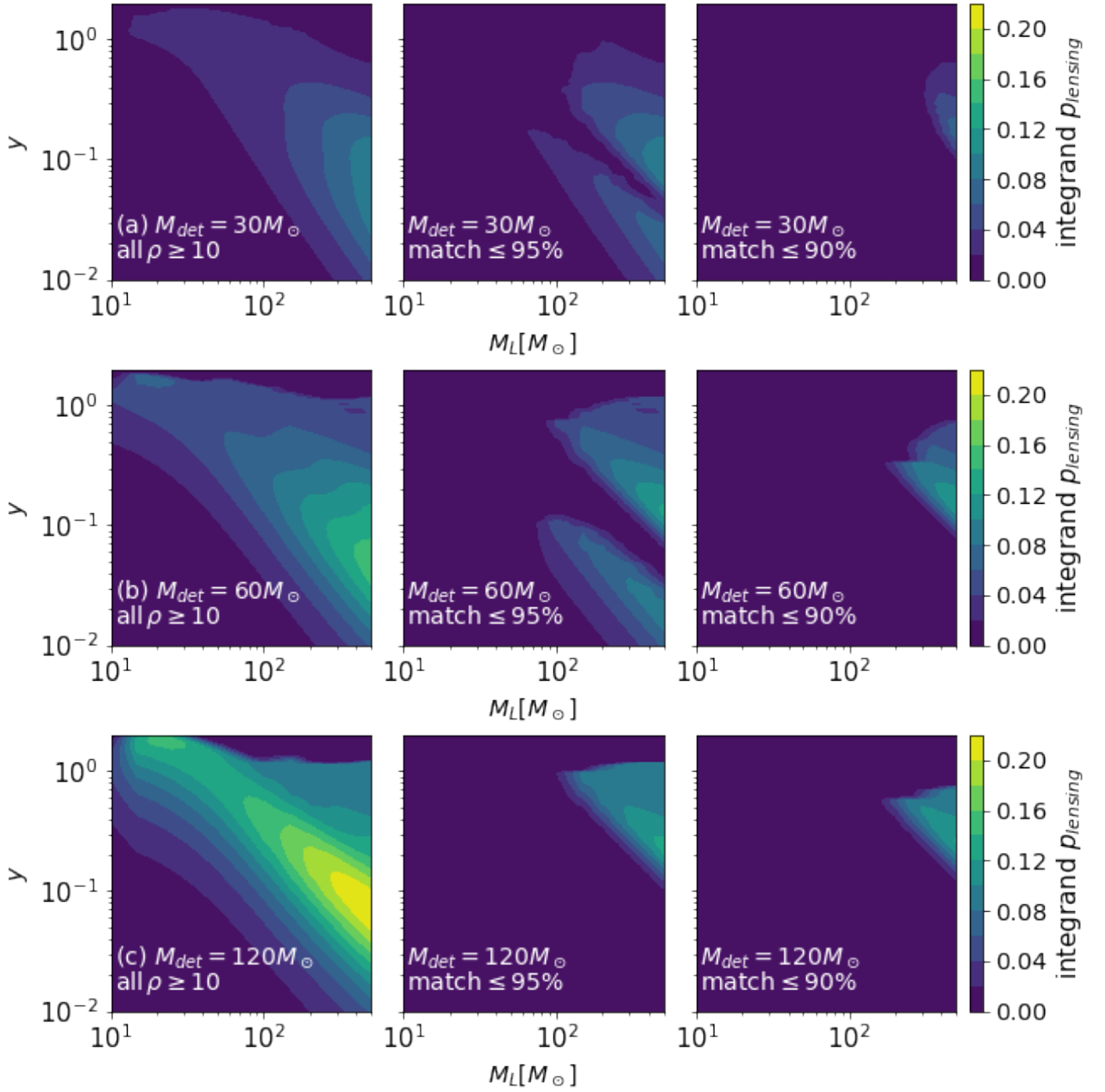


FIG. 10: Probability density as a function of y and M_L for black hole binaries of total detected mass (a) $M_{det} = 30M_\odot$, (b) $M_{det} = 60M_\odot$ and (c) $M_{det} = 120M_\odot$ for all sources of $\rho \geq 10$. The first column plots all lensed sources, the second the lensed sources with a mismatch of 5% or greater, and the third the lensed sources with a mismatch of 10% or greater. All are scaled by the total number of sources. The GO average and amplification only regions separate for intermediate mismatch $\geq 5\%$ (subfigures a and b). It can be seen that the most lensed sources occur for $M_{det} = 120M_\odot$. While many sources may be lensed only the fraction of them that have detectable mismatch with unlensed templates can be identified as lensed by LVK searches.

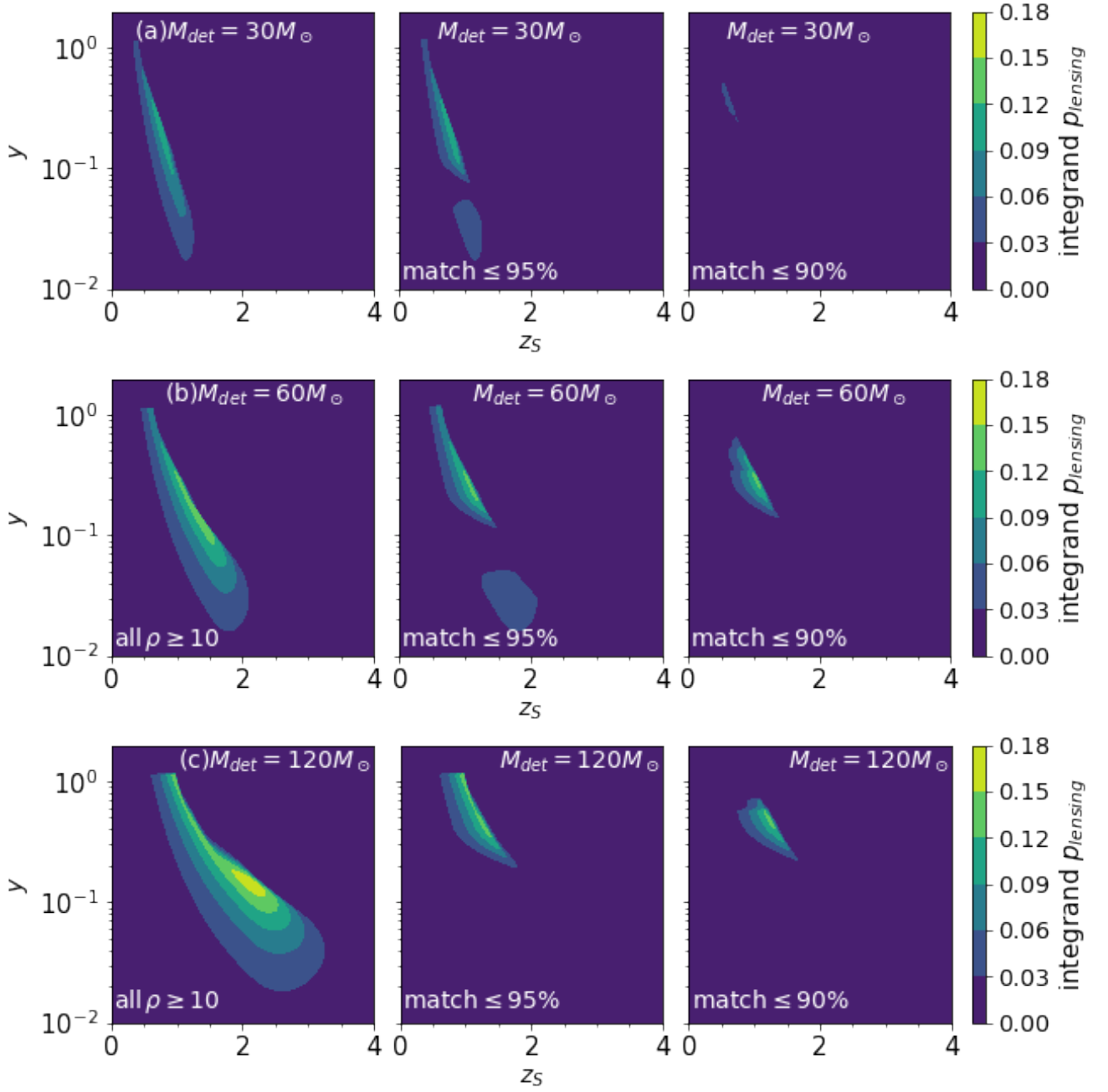


FIG. 11: Probability density of $M_L = 300M_\odot$ as a function of y and z_S for black hole binaries of total detected mass (a) $M_{det} = 30M_\odot$, (b) $M_{det} = 60M_\odot$ and (c) $M_{det} = 120M_\odot$ for all sources of $\rho \geq 10$. The first column shows all lensed sources, the second the lensed sources with a mismatch of 5% or greater, and the third the lensed sources with a mismatch of 10% or greater. All are scaled by the total number of sources. Like before it can be seen that the most lensed sources occur for $M_{det} = 120M_\odot$ which can be seen up to $z \approx 3.2$, and that only a small number of sources have a mismatch of 5% or more ($z_S < 2$). When the mismatch increases to 10% or more, the amplification only region disappears.

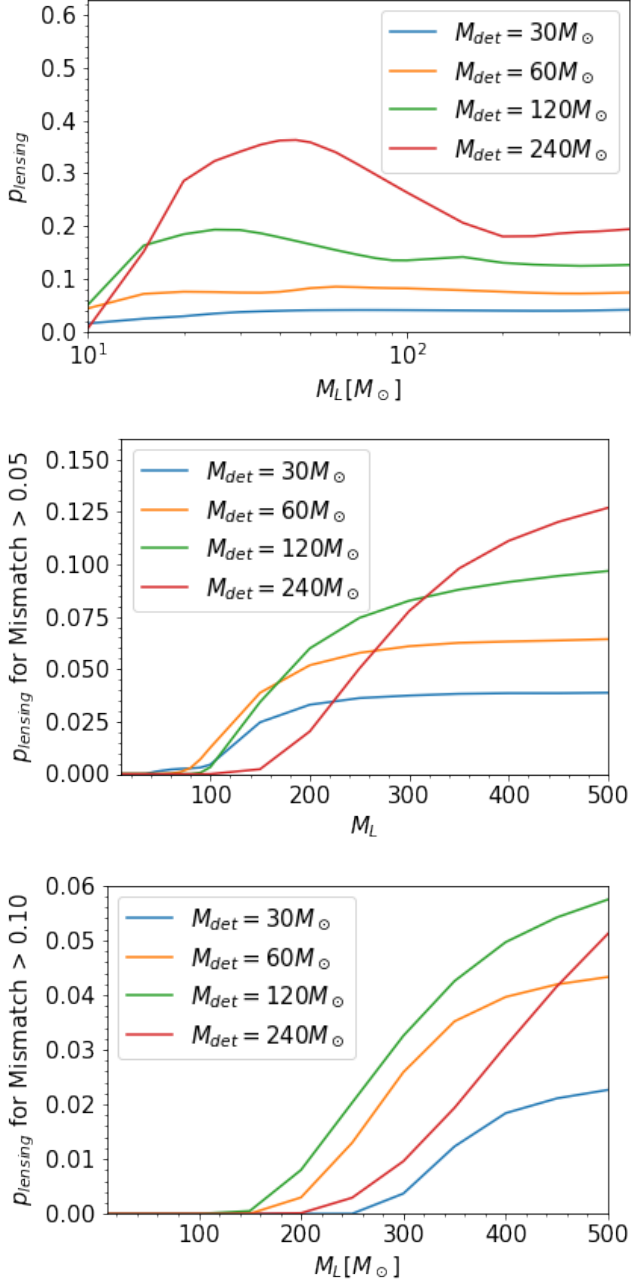


FIG. 12: Probability of lensing integrated over all y shown a function of M_L for (a) all lensed sources, (b) lensed sources with a mismatch $\geq 5\%$ (c) lensed sources with a mismatch $\geq 10\%$ for black hole binaries of total detected mass $M_{det} = 30M_\odot$, $M_{det} = 60M_\odot$, $M_{det} = 120M_\odot$ and $M_{det} = 240M_\odot$ computed for $\rho \geq 10$. It can be seen lensing becomes discernible with the LVK only for $M_L \gtrsim 300M_\odot$ with less than 10% of lensed events identifiable as lensed.